Publication Year	2024
Acceptance in OA	2025-04-03T09:39:50Z
Title	In situ observations of large-amplitude Alfvén waves heating and accelerating the solar wind
Authors	Rivera, Yeimy J., Badman, Samuel T., Stevens, Michael L., Verniero, Jaye L., Stawarz, Julia E., Shi, Chen, Raines, Jim M., Paulson, Kristoff W., Owen, Christopher J., Niembro, Tatiana, Louarn, Philippe, Livi, Stefano A., Lepri, Susan T., Kasper, Justin C., Horbury, Timothy S., Halekas, Jasper S., Dewey, Ryan M., DE MARCO, Rossana, Bale, Stuart D.
Publisher's version (DOI)	10.1126/science.adk6953
Handle	http://hdl.handle.net/20.500.12386/37008
Journal	SCIENCE
Volume	385

Science
AAAS

Supplementary Materials for

In situ observations of large amplitude Alfvén waves heating and accelerating the solar wind

Yeimy J. Rivera*†, Samuel T. Badman†, Michael L. Stevens, Jaye L. Verniero, Julia E. Stawarz, Chen Shi, Jim M. Raines, Kristoff W. Paulson, Christopher J. Owen, Tatiana Niembro, Philippe Louarn, Stefano A. Livi, Susan T. Lepri, Justin C. Kasper, Timothy S. Horbury, Jasper S. Halekas, Ryan M. Dewey, Rossana De Marco, Stuart D. Bale

* Corresponding author: yeimy.rivera@cfa.harvard.edu

† These authors contributed equally to this work

The PDF file includes:

Materials and Methods

In situ observations

For Parker, we examined observations from the Solar Wind Electrons Alpha and Protons instrument suite (SWEAP, (*40)*) to compute proton and alpha particle number densities, temperatures, and bulk velocities. Specifically, we used the Solar Probe Analyzer - ions instrument (SPAN-I, (*41*)) instrument which couples an electrostatic analyzer and time-of-flight (TOF) component to resolve incident angle, mass-per-charge, and energy-per-charge of incoming ions. The mass discrimination by the TOF analyzer allows for the identification of separate ions species in the solar wind, mainly the most abundant species -- protons and alpha particles. SPAN-I provides individual 3D particle distributions of proton and alpha particles. However, due to partial obstruction to the instrument by the heat shield and solar panels, the SPAN-I field-of-view (FOV) is partially blocked on the ecliptic plane, only measuring partial distributions. We discuss the treatment of the SPAN-I observations in the following section. We included electron measurements from Solar Probe Analyzer - electrons instrument (SPAN-e, (*42*)*)*, extracting estimates of the electron temperature and electron heat flux using a previously described methodology (*43*). The three dimensional (3D) magnetic field components were measured by the fluxgate magnetometer on the Electromagnetic Fields Investigation suite (FIELDS, (*44*)) at 4 vectors per spacecraft clock cycle that captures the rapid changes in the magnetic field.

For Solar Orbiter, measurements of the magnetic field were taken by the Solar Orbiter magnetometer (MAG, (*45*)) at 8 vectors s^{-1}. Observations of protons, alpha particles, and heavier ions across this period were taken by the Proton-Alpha System (PAS) and Heavy Ion Sensor (HIS, (*46*)) instruments that are part of the Solar Wind Analyzer suite (SWA, (*47*)) suite. The proton and alpha densities, temperatures, and velocities were measured with the PAS instrument with 4s full scan 3D particle distributions. Properties of the alpha population were determined from the PAS measurements using a machine learning statistical clustering technique (*48*). Observations of the heavier ions (atomic number, $Z > 2$) were accumulated at a 10 minute resolution using the time-of-flight mass spectrometer, HIS.

The raw time series measurements of magnetic field and solar wind speed from Parker/FIELDS and SWEAP and Solar Orbiter/SWA and MAG are shown in Figure S1.

SPAN-Ai measurements analysis

The 3D plasma parameters of the proton core and beam populations at Parker were obtained in two ways, (1) by fitting a double bi-Maxwellian model to the observed proton velocity distribution functions (VDF) (a level 2 SWEAP data product), and (2) by using

the instrument provided particle moments (a level 3 SWEAP data product). We summed 8 distributions together which provided a ~30s cadence. The best-fitting models were used as validation for the density and temperature moments. We verified they were not impacted by SPAN-I's FOV by re-computing the plasma moments using the best-fitted values as input. Since the density moment is most affected by part of the VDF being outside of the FOV, we then divided the fitted density moment by the sum of the fitted core and beam density. This gives a rudimentary measure of the SPAN-I FOV fraction, between 0 and 1, at each time step. The median value over the interval of interest (2022 February 25, 15:00 to 16:40) was 0.95, indicating that it is appropriate to use the proton moments in this time interval. We cross-compared the measured proton density moment to the electron density as determined by fits to the electron VDFs (*49*) and verified that the values match and the plasma is approximately quasi-neutral.

The effective isotropic temperature (T) was computed as the trace of the temperature tensor moment (T_{ij}) divided by 3, where the subscripts (i,j) take the values of x, y and z, the cartesian components of the SPAN-I instrument coordinate frame.

Ballistic Mapping

During Parker's 11th solar encounter (designated E11), the spacecraft was in close conjunction with Solar Orbiter for a period centered on 2022 February 25. Figure 1 shows (in the solar-corotating (Carrington) frame) the streams projected into the heliographic equatorial plane with the trajectories ballistically mapped *(22,23,24)* to an altitude of 2.5 $R_\odot$. The ballistic mapping method utilizes the heliographic location of the spacecraft (Fig. 1.), and the measured solar wind velocity (Fig. S1 C,D), to define an archimedean spiral field which approximately traces the path of the relevant plasma parcel (when viewed in the solar co-rotating frame in Figure 1) back to its origin in the outer corona.

Parker measured this stream over two hours on the afternoon (UTC) of 2022 February 25 (1500-1640 UTC), while measurements from Solar Orbiter of the same stream took place on February 27 2022 (0900-1700 UTC) (Fig S1).

We sample the spacecraft 3D heliographic position at the cadence of the SPAN-i and PAS measurements (for Parker and Solar Orbiter respectively) then apply equation 3 in *(23)* to the measured velocity to produce a mapped heliographic spacecraft location at 2.5 $R_\odot$ as a function of time (Fig. 1B). This provides a transformation of the timeseries measurements to a function of longitude (Fig. 2). To combine measurements between instruments on each spacecraft the longitude vs. time data is linearly interpolated to the same measurement cadence, which for each spacecraft is chosen to be the cadence of the velocity measurements.

A ballistic solar wind speed based on an asymptotic value far from the Sun may appear a poor representation of the trajectory of an accelerating parcel, it results in a mapping closer to the true source than an accelerating streamline would (from >9 degrees to <3 degrees when mapped from 1au *(26)*, and smaller for mapping from closer to the Sun). This is because the integrated effect of co-rotational torques relative to the ballistic trajectory is to tighten the spiral which opposes the net effect of the acceleration, which acts to make it less tightly wound; the integral of these effects nearly cancels out *(24, 25, 26)*. We perform mapping for both spacecraft down to 2.5 $R_\odot$.

Parker and Solar Orbiter move in opposite heliographic directions (Fig. 1.), and cross the same streams in reverse order at different heliocentric distances (13.3 and 127.7 $R_\odot$ respectively). Figure 1B shows the ballistically mapped source surface longitude which we use to compare Parker and Solar Orbiter data. The region of fast wind we selected contains a switchback patch *(14)*. This conjunction occurs when Parker and Solar Orbiter are also nearly coincident in latitude; other spacecraft conjunction intervals in the heliosphere have greater latitudinal offset.

When there are strong velocity gradients, ballistic mapping can indicate that field lines from neighboring fast and slow streams cross each other which is unphysical. However, for an individual stream of similar velocity we regard this method as a sufficient approximation, especially for spacecraft close to the Sun. Ballistic mapping provides similar source connectivity predictions to methods which do include stream interactions (*50*).

Estimate of transit time

We estimate the transit time of the measured plasma parcel from Parker to Solar Orbiter (Δt ~ 45 hours) and find that it is close to the delay in which Solar Orbiter crosses the stream relative to Parker (~40 hours).

To make this estimate, we utilize the solar wind model described below and plotted in Figure 4. Specifically, we take the model profile of the velocity depicted in Figure 4C, ($u(R)$), and numerically compute the following integral over heliocentric distance (r) from Parker (R_{Parker}) to Solar Orbiter ($R_{\text{Solar Orbiter}}$):

$$\Delta t = \int_{R_{Parker}}^{R_{Solar\ Orbiter}} 1/u(r)\, dr \quad \text{(Eqn S1)}$$

Obtaining average stream properties

Once transformed to a function of longitude, the stream of interest at both spacecraft is identified as the region of data from 120°-125° longitude. To derive averages and

standard deviations across this stream, we uniformly sampled in longitude, splitting the 5 degree interval into 205 equally spaced bins by averaging all data points in each bin (typically 500 data points).

For Solar Orbiter, we rejected data from a neighboring stream in the population of measurements from 120-122 deg by identifying a bifurcated signature in Helium abundance (Fig. 2K). Measurements of plasma properties in this longitude range with a corresponding helium abundance > 2.5% were removed prior to computing the averages and standard deviation.

The values reported in Tables S1 and S2 and plotted in Figures 3 and 4 are the mean and standard deviation of this uniformly sampled dataset across longitude with the helium abundance-based filter applied.

Mass and magnetic flux conservation

We investigate the mass flux and magnetic flux conservation of the stream. Overall, the stream exhibits small non-radial underexpansion in which mass flux is slightly increased at Solar Orbiter relative to Parker and correspondingly is threaded by a slightly larger magnetic flux by factors of 11% and 10% respectively (where both quantities are weighted by the square of the heliocentric distance). We track this underexpansion to determine the energy fluxes measured at Solar Orbiter listed in Table S2, plotted in Figure 3, and in comparing energy fluxes to the modeling in Figure 4D.

Mass flux conservation between Parker and Solar Orbiter is governed by the equation:

$$\frac{dM}{dt}\Big|_{Solar\ Orbiter} - \frac{dM}{dt}\Big|_{Parker} = (\Omega n_p u_{cm} r^2)_{Solar\ Orbiter} - (\Omega n_p u_{cm} r^2)_{Parker} = 0 \quad \text{(Eqn S2)}$$

Where Ω is the flux tube angular size in steradians, n_p is the proton number density, v_p is the proton bulk velocity and r is the heliocentric distance.

Using the characteristic values in Table S1, we calculate mass conservation as

$$f = \Omega_{SolarOrbiter} / \Omega_{Parker} = \frac{(n_p u_{cm} r^2)_{Parker}}{(n_p u_{cm} r^2)_{SolarOrbiter}} = 0.90 \pm 0.090 \text{ (Eqn S3)}$$

This indicates that the tube is approximately conical but has under expanded by a factor of ~10%. We therefore set the flux tube expansion factor, $f = 0.90 \pm 0.090$ between the 0.53 au spacecraft separation. For comparison, a previous analysis of a ~ 600 km/s coronal hole stream from *(17)* found a value of $f \sim 0.88$ for two spacecraft separated by 0.2 au between 0.5 to 0.7 au from the Sun in line with the present study.

We also investigate whether the expansion implied by conservation of mass and magnetic flux across the flux tube to verify that the mass flux is balanced by magnetic flux conservation. Because this environment is confined to a single magnetic sector of positive polarity, we do not expect any annihilation. We relate the magnetic flux scaling of $B_r\ r^2$ = constant to $n_p v_p r^2$= constant, so $g = n_p v_p / B_r$ = constant. Using the average values from Table S1, we compute a ratio of $g_{Parker}/g_{Solar\ Orbiter}$ = 1.01 ± 0.16. A value close to 1 indicates that magnetic flux and mass are balanced in the flux tube segment between the two spacecraft. Figure S2 shows the variation in mass and magnetic flux conservation across the source surface longitude range 120–125 degrees.

Energy flux conservation

The conservation of energy in equations 1-3 was expressed in terms of energy densities, U_K, U_H, U_G, U_w (respectively kinetic, enthalpy, gravitation and Alfvén waves). These terms are expressed in terms of measured quantities as:

$$U_K = \Sigma_j \frac{1}{2} m_j n_j (u_{cm})^2 \qquad \text{(Eqn S4a)}$$

$$U_H = \Sigma_j \frac{5}{2} n_j k_B T_j \qquad \text{(Eqn S4b)}$$

$$U_G = \Sigma_j \frac{n_j m_j G M_\odot}{R_\odot} (1 - R_\odot / r) \qquad \text{(Eqn S4c)}$$

$$U_W = (3/2 + V_A / u_{cm}) \frac{\delta B^2}{2\mu_0} \qquad \text{(Eqn S4d)}$$

In Equation S4a-d, Σ_j indicates a sum over each significant species (j) in the plasma (protons, electrons, and alpha particles). r is distance from the Sun in units of solar radii. The number density, mass, and temperature for particles of species j are given by n_j, m_j, and T_j, respectively. V_A is the local Alfvén speed. G, k_B, $M_\odot$, $R_\odot$, μ_0, are the gravitational constant, Boltzmann constant, solar mass, solar radius, and permeability of free space, respectively. The plasma center of mass velocity (u_{cm}) is defined in the main text. In equation S4d, δB is computed as the magnetic field deviation from the mean field, where $\delta B_r = |B_{r,i} - \langle |B| \rangle_t \cos(\varphi)|$ and $\delta B_{n,i} = B_{n,i}$, $\delta B_{t,i} = |B_{t,i} - \langle |B| \rangle_t \sin(\varphi)|$, where $B_{x,i}$ is the associated component at each time step, i, and $\langle |B| \rangle_t$ is the magnitude of the field averaged over 10 minute intervals, t, at Parker and Solar Orbiter, and $\delta B = (\delta B^2_r + \delta B^2_t + \delta B^2_n)^{1/2}$. φ is the spiral angle and assumed to be zero at Parker (radial background field) and 25 degrees at Solar Orbiter. The definition of the Alfvén wave energy flux *(34)* includes the energy contribution both in the magnetic and velocity fluctuations associated with the switchback patch.

Equations 1-3 show how these quantities are used to express energy conservation in terms of energy fluxes. The energy conservation equation is only valid under the assumption of radial mean flow and magnetic field. Each respective energy density measurement is multiplied by the flux tube subtended area ($r^2\Omega$) and center of mass velocity (u_{cm}). This gives the energy fluxes W_K, W_H, W_G, W_w in Equation 2, Figures 3 and 4 and in Table S2.

We do not include the electron and proton heat flux in the energy flux terms because their contribution is negligible compared to other energy terms (c.f. Table S2), 0.1 W m^{-2} and 0.008 W m^{-2}, respectively.

Polytropic solar wind modeling

Figures 4A, C, D and S3 show a model of the solar wind *(29,30)*. We adopt an isothermal solution *(29)* of constant temperature T_0 out to some radius R_{iso} *(5,6)* outside which we constrain the solar wind to cool with an empirically determined polytropic index $1< \gamma \leq 5/3$. We introduced a data-constrained force profile to investigate direct forcing by a gradient in Alfvén wave pressure. The model implementation and functional form of the forcing explicitly follows *(5)*. The forcing term and how it is constrained are discussed further below. See [*(5)* their section D] for a complete description of the hydrodynamic equations solved here. The model solutions are generated using code available at https://www.github.com/STBadman/ParkerSolarWind and archived in a Zenodo repository (39). The temperature measurements (Fig 4A) constrain the polytropic index to $\gamma = 1.41 \pm 0.020$ and permit a range of values of (T_0, R_{iso}) with the qualitative relationship that a lower isothermal radius implies a larger coronal temperature. The uncertainty in γ is estimated conservatively by determining the maximum and minimum values beyond which the temperature profile no longer falls within 1σ error bars of the temperature measurements. With only thermal pressure gradients, we find no solutions that match the acceleration of the solar wind between Parker and Solar Orbiter for this stream, even allowing for unphysically high coronal temperatures. We therefore investigated whether quantifying wave forcing could resolve this discrepancy.

We fitted a model force profile to measurements of the Alfven wave pressure gradient following an analytical construction from [*(5)*, their section D]. This represents force per unit mass ($F(r)$) as a function of heliocentric distance (r).

$$F(r \mid f_0, \alpha, \beta) = f_0 \frac{1 + \beta(r/R_0 - 1)}{(r/R_0)^2} exp[\alpha(1 - R_0/r)] \quad \text{(Eqn S5)}$$

Where f_0 sets the overall strength of the profile in units of $GM_\odot/R_\odot^2$, $R_0 = 1R_\odot$ and [α = 0.2, β = 74] set the location of maximum force. The values of α and β were chosen to result in a maximum in the low corona, but our results are insensitive to this choice unless the resulting model violates the data constraints (see below). The square exponent in the denominator of the second term in equation S5 causes asymptotic behavior of F(r) ∝ $1/r^2$ at large *r* which matches the data (Fig 4B) and sets f_0. We approximate the wave energy content in the stream as dominated by radially outwards propagating Alfvén waves from switchbacks whose wave pressure (P_w) at Parker and Solar Orbiter therefore depends only on the measurement δB. The analytical force is constrained directly *(34)*:

$$F(r) = -(1/2\rho(r))(\nabla \cdot P_w)_r = -(1/2\rho(r))\frac{d}{dr}(\delta B^2(r)/2\,\mu_0) \quad \text{(Eqn S6)}$$

where the minus sign reflects that the force the plasma feels is of the opposite sign to the wave pressure gradient, and ρ(*r*) is the measured mass density. The constraint requires an estimate of the wave pressure gradient. We use the two independent measurements of P_w from Parker and Solar Orbiter and assume a power law decay based on recent measurements of wave energy flux decay with distance from 13.3Rs outwards *(4),* from one to the other. We use the gradient of the fitted power law to derive a measurement of the wave pressure force from Parker and Solar Orbiter. We then performa least-squares fit to f_0 to match these two measurements and their uncertainties resulting in the force profile plotted in Figure 4B which has parameters f_0=0.012 ± 0.0020, α=0.2, β =74 .

Due to the low Alfvén Mach number regime where the wind is accelerating, the force profile implies a faster decrease in wave pressure compared to theoretical expectations (*34)*. We consider the decay of outwards radially propagating Alfven waves under conservation of wave action [(*34),* their equation 40]. This equation describes how the energy density of such waves ($E_D(r)$ in Equation S7 where D denotes 'dissipation-free') depends on heliocentric distance (*r*), Alfven speed (V_A) and flow speed *u* (which are both themselves functions of radius):

$$E_D(r) \propto V_A(r)/[r^2(u(r) + V_A(r))^2] \quad \text{(Eqn S7)}$$

The force per unit mass imparted by these dissipation-free waves (F_D) is proportional to $(1/\rho(r))\ d/dr\ E_D(r)$. Under the limits $u >> V_A$ and $u \sim$ const (as is the case far from the Sun), we find $E_D(r) \propto V_A/r^2$, $\rho(r) \propto 1/r^2$ and $V_A \propto B_R(r)/\sqrt{\rho(r)} \propto 1/r$ (assuming global conservation of magnetic flux). Combining these, we obtain the asymptotic behavior $F_D(r) \propto r^2\ d/dr\ (1/r^3) \propto 1/r^2$.

However, for the evolution in the measured stream (Figure 4), neither of the asymptotic limits are satisfied, so we expect the profile to follow Equation S7, including its detailed functional dependence of $u(r)$ and $V_A(r)$. This leads to a radial force profile $F_D(r)$ which starts flatter in the accelerating regime and steepens to asymptote to $1/r^2$. This is shown by plotting with known functions of $u(r)$ and $V_A(r)$ from the solar wind models presented in Figure 4 (assuming $B_r(r) \propto 1/r^2$). In Figure 4B, we show a reference profile of an expected force profile that matches the amplitude of fluctuations measured at Parker. We find that the observed decay in wave pressure is steeper. This causes the integral of the force profile from Parker to Solar Orbiter to use only a fraction of the available wave energy flux.

The fitted force profile and polytropic index, along with the mass flux normalization (via setting a reference density n_0) constrains the solar wind model from Parker out to Solar Orbiter. However it does not explain the acceleration of the solar wind between the corona and Parker. We model this by setting a critical point in the corona and adjusting its altitude. We do this by extrapolating the fitted force profile down to $1R_\odot$ using equation S5 and varying T_0 and R_{iso} (see Fig. 4).

Our final model matches the evolution from Parker to Solar Orbiter: Simultaneously, the core proton temperature cools from ~1.4MK to ~0.23 MK, the solar wind accelerates from ~384 km/s to ~512 km/s, and the proton density dropping by a factor of 100.

The model parameters are R_{iso} = 11.0 $R_\odot$ and T_0 = 1.7MK, consistent with ultraviolet observations of fast solar wind proton temperatures (Fig. 4A) *(31).* and in combination with the extrapolated force profile results in a critical point at 2.2 $R_\odot$. The continuation of the wave force profile into the corona provides an additional 20 W m^{-2} of energy flux into the budget, sufficient to match the observed initial solar wind speed measured at Parker. This value was determined from the model in Fig. 4D, with and without the wave force, by computing the total addition to the energy flux in both cases.

Any other acceleration process that produces the same velocity at Parker would lead to the same heliospheric evolution under the same heliospheric forcing and polytropic index (which are well constrained by the measured data).

Supplementary Text

Polytropic index

The temperature measurements constrain the polytropic index for this stream to γ=1.41 ± 0.020, implying less temperature evolution than would be expected for the adiabatic case γ = 5/3 ~ 1.66. The polytropic index we obtained is similar to that obtained in previous work [*(6)* their solution D with ~ 500 km/s at 1 au and γ ~1.44]. This value requires an isothermal layer (or other method of solar wind forcing) (5), since a continued polytropic index of 1.41 all the way to $1R_\odot$ would not have a valid solar wind solution (and the implied temperature in the low coronal would be unphysically high). The solar wind must cross its sonic point (R_c) within the isothermal layer, which places a lower bound of $R_{iso} > R_c$ within this model framework, which is satisfied by the model parameters here ($R_{iso} = 11.0\ R_\odot$, $R_c = 2.2\ R_\odot$).

Compositional constraints on the stream source

We use heavy ion composition measurements from Solar Orbiter to investigate the source of the stream. Figure S4 shows the Fe/O elemental ratio normalized by its photospheric ratio, Fe/O_{phot} ~ 0.06 (*51*), measured for the switchback patches with source surface longitude 120-125. These indicate an enhanced (relative to photospheric abundance) first ionized potential (FIP) value of $[Fe/O]/[Fe/O]_{phot}$ =2.3±0.15. This Fe FIP bias is characteristic of fast, coronal hole solar wind (*52*). The low n_{He}/n_p (~1%) abundances in the solar wind stream correspond to slower speed, streamer belt wind at solar minimum (*53*). The n_{He}/n_p ratio we measure is inconsistent with previous studies which found higher He abundance within switchback patches (~4%) than solar wind in which they are embedded (~1%) *(14).* Not all switchback periods are characterized by enhancements in He abundance, even between neighboring patches across a single perihelion encounter *(54, 55)*. Variability among switchback He abundance could be due to differing sources at the Sun. Deviation from the typical He to Fe composition trends of coronal hole wind indicates a mixture of open and closed solar sources, as predicted by models of interchange reconnection, in line with some models of their formation (*56, 57, 58*). The specific coronal hole sources implied by modeling this encounter of this stream (Fig. 2F and L) are thin, extended and equatorial, consistent with closed and open field lines in close proximity at the source.

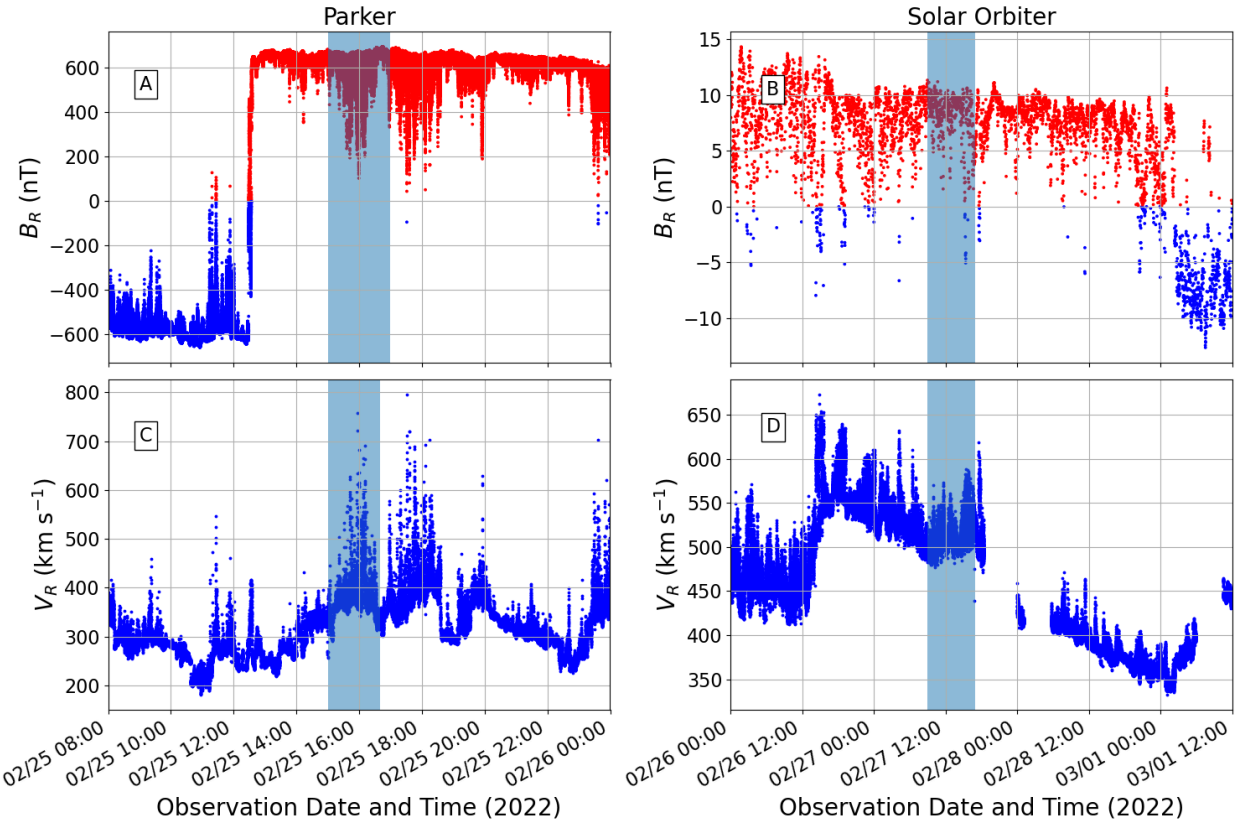

Figure S1. Time series of mapped stream. Panel A and B show the observed radial magnetic field measured by Parker Solar Probe and Solar Orbiter respectively as a function of time. Red and blue colorization respectively highlights intervals of predominantly positive and negative magnetic polarity. Panel's C and D show the observed radial velocity for the same time intervals. The blue vertical shading in all panels shows the times corresponding to the mapped stream. The time interval corresponding to the patch at Parker is less than 2 hours (2022 February 25, 1500 to 1640 UTC) in duration compared to 8 hours at Solar Orbiter (2022 February 27 0900 to 1700 UTC) due to the differing spacecraft angular velocity in the solar co-rotating frame. Black markers show hourly medians used to do the ballistic mapping.

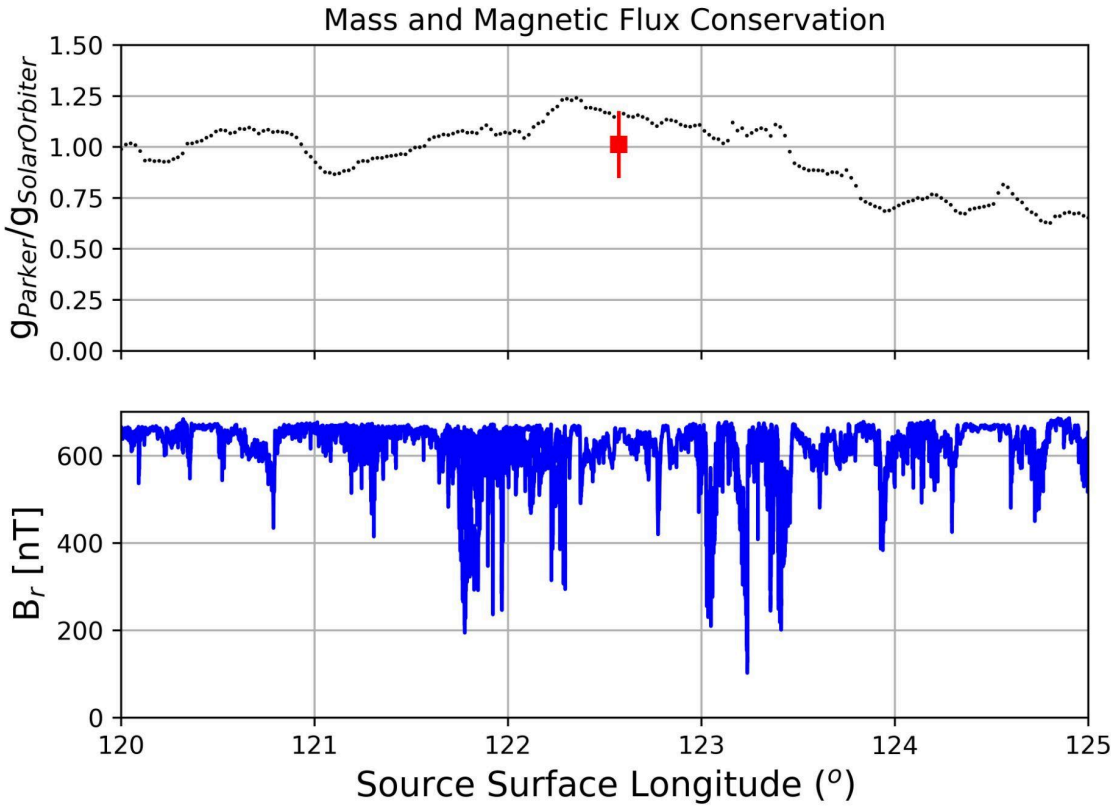

Figure S2. Mass and magnetic flux conservation across the stream and switchback patch as a function of source surface longitude. Panel A shows the ratio of $g = n_p v_p / B_r$ measured at Parker and Solar Orbiter across the stream. The mean and standard deviation of 1.03 ± 0.16, is plotted in red. Panel B shows the radial component of the magnetic field at Parker Solar Probe in the stream showing the presence of the Alfvénic switchbacks observed as large downward spikes in the data towards zero. The mean flux ratio plotted in A is consistent with the value of 1.0 expected from energy conservation.

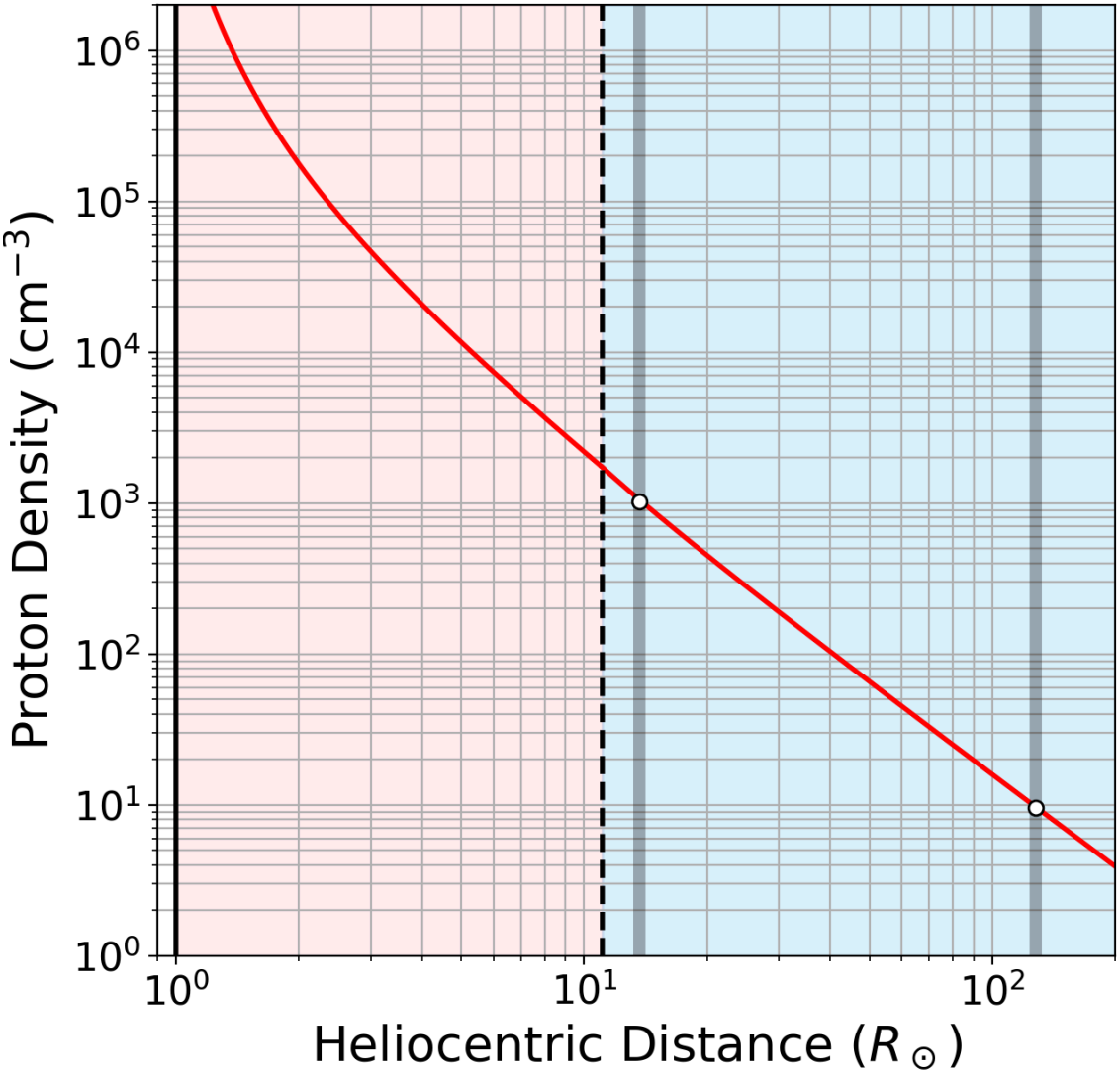

Figure S3. Same as Fig 4C, but for the proton density. Red curve shows the model solution while white data points show the constraints taken from measurements by Parker and Solar Orbiter. Error bars are smaller than the data points.

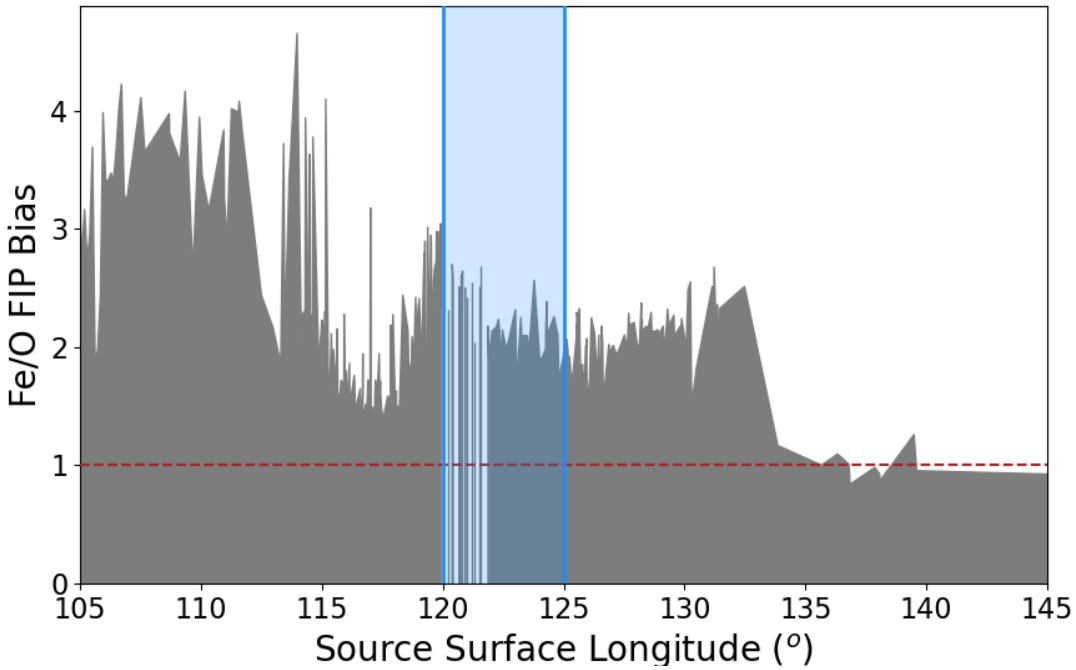

Figure S4. First Ionization Potential (FIP) Bias measured by Solar Orbiter as a function of source surface longitude. The grey filled curve shows the measured relative abundance of iron to oxygen, as a fraction of the typical ratio in the photosphere (the Fe/O FIP Bias). A brown dashed horizontal line indicates photospheric abundances. Blue shading indicates the location of the stream studied in this work and demonstrates an enhancement compared to photospheric abundances typical of coronal hole fast wind.

Table. S1. Mean measured properties of the solar wind stream at Parker and Solar Orbiter between source surface longitude 120-125. For Solar Orbiter, we exclude values associated with an overlapping stream between source surface longitude of 120-122 associated with a helium abundance of 3% (n_{He}/n_p ~0.03, see Figure 2K). We only considered plasma that matched the Parker Solar Probe helium abundances of 1% (Figure 2E). Quoted uncertainties are 1 sigma. * Electron temperature at Solar Orbiter is estimated from the measured proton temperature assuming the same proton to electron temperature ratio measured at Parker.

Properties	Parker Solar Probe	Solar Orbiter
n_p [cm^{-3}]	1026 ± 86	9.6 ± 1.1
V_p [km s^{-1}]	386 ± 26	512 ± 15
T_p [MK]	1.36 ± 0.15	0.204 ± 0.028
V_A [km s^{-1}]	435 ± 21	71.5 ± 3.6
B_r [nT]	624 ± 42	7.9 ± 2.0
|B| [nT]	668.0 ± 4.5	10.2 ± 0.6
n_α [cm^{-3}]	13.2 ± 5.2	0.090 ± 0.020
v_α [km s^{-1}]	541 ± 68	585 ± 28
T_α [MK]	13.7 ± 3.7	0.74 ± 0.20
T_e [MK]	0.470 ± 0.010	0.078 ± 0.024 *
δB [nT]	202 ± 100	7.2 ± 2.6

Table. S2. Energy terms within the stream. The values are computed for both spacecraft using Equations 2 & S4 averaged across source surface longitude 120–125 deg, normalized by the flow speed and scaled to $1R_{\odot}$. The values in parentheses are the totals excluding the wave energy flux (W_w). The values of Solar Orbiter are multiplied by an expansion factor, *f*, from the mass conservation calculation (see materials and methods). Uncertainties indicate the standard deviation of all measurements within the stream. The bottom right entry in the table indicates energy conservation is achieved when accounting for W_w.

Energy Flux Terms	Parker Solar Probe [W m^{-2}]	Solar Orbiter [W m^{-2} × f]	Δ Solar Orbiter - Parker
W_K	10.7 ± 2.0	18.8 ± 1.4	8.1 ± 2.4
W_H	5.70 ± 0.84	0.75 ± 0.12	-4.95 ± 0.85
W_G	25.1 ± 2.2	28.5 ± 2.1	3.4 ± 3.0
W_w	4.1 ± 2.9	0.25 ± 0.07	-3.9 ± 2.7
Total	45.7 ± 6.6 (41.5 ± 4.5)	48.0 ± 3.6 (47.8 ± 3.5)	2.3± 7.5 (6.2 ± 5.6)